

DA-Occ: Direction-Aware 2D Convolution for Efficient and Geometry-Preserving 3D Occupancy Prediction

Yuchen Zhou^a, Yan Luo^a, Xiaogang Wang^b, Xingjian Gu^{*a}, Mingzhou Lu^a, Xiangbo Shu^c

^aNanjing Agricultural University, guxingjian@njau.edu.cn, Nanjing, 210095, Jiangsu, China

^bDesay SV Automotive co.,LTD., , Nanjing, 210095, Jiangsu, China

^cNanjing University of Science and Technology, , Nanjing, 210095, Jiangsu, China

Abstract

Efficient and high-accuracy 3D occupancy prediction is crucial for ensuring the performance of autonomous driving (AD) systems. However, many existing methods involve trade-offs between accuracy and efficiency. Some achieve high precision but with slow inference speed, while others adopt purely bird’s-eye-view (BEV)-based 2D representations to accelerate processing, inevitably sacrificing vertical cues and compromising geometric integrity. To overcome these limitations, we propose a pure 2D framework that achieves efficient 3D occupancy prediction while preserving geometric integrity. Unlike conventional Lift-Splat-Shoot (LSS) methods that rely solely on depth scores to lift 2D features into 3D space, our approach additionally introduces a height-score projection to encode vertical geometric structure. We further employ direction-aware convolution to extract geometric features along both vertical and horizontal orientations, effectively balancing accuracy and computational efficiency. On the Occ3D-nuScenes, the proposed method achieves an mIoU of 39.3% and an inference speed of 27.7 FPS, effectively balancing accuracy and efficiency. In simulations on edge devices, the inference speed reaches 14.8 FPS, further demonstrating the method’s applicability for real-time deployment in resource-constrained environments.

Keywords: Autonomous Driving, 3D Occupancy Prediction, Bird’s-Eye View, Direction-Aware Convolution

1. Introduction

Autonomous driving systems in intelligent transportation environments rely critically on accurate and timely perception of the surrounding 3D scene Arnold et al. (2019); Zhu et al. (2017). In this context, vision-based occupancy prediction has emerged as a key approach that estimates both object occupancy and semantic information in a 3D voxel space from surround-view images captured by vehicle-mounted cameras Cao and De Charette (2022); Tian et al. (2023); Li et al. (2023b,c). Accurate 3D geometry and semantic understanding of the surrounding environment are essential for autonomous driving (AD) Wu et al. (2024). Compared to conventional 3D object detection Liang et al. (2022); Yin et al. (2021), occupancy prediction provides finer-grained 3D scene understanding and is capable of recognizing general objects by learning their occupancy patterns.

Occupancy prediction offers several advantages, including improved scene understanding, improved handling of unknown obstacles, and joint modeling of geometry and semantics modeling. However, many existing methods Ma et al. (2024); Wei et al. (2023); Huang et al. (2021); Wu et al. (2024) focus primarily on precision, often at the expense of real-time processing due to the complexity of their model architectures and large parameter counts. Consequently, these methods suffer from high computational costs and latency, making them impractical to implement in real-time autonomous driving (AD) systems He et al. (2025). To ensure real-time inference speed and facilitate



Figure 1: The inference speed (FPS) and accuracy (mIoU) of various methods are evaluated on the Occ3D-nuScenes benchmark Tian et al. (2023). Following the convention in Hou et al. (2024), 10 FPS is often treated as a relaxed real-time threshold. In this work, we additionally consider stricter operating points (e.g., 15 FPS and 20 FPS) to better reflect safety-critical autonomous driving scenarios.

deployment, some approaches adopt 2D methods to predict 3D voxel occupancy Park et al. (2025); Li et al. (2023c); Yu et al. (2023); Li et al. (2025); Hou et al. (2024). These methods typically compress 3D voxel features into bird’s-eye view (BEV) representations, retaining only horizontal information. As a result, certain semantic and vertical geometric details are sacrificed, even at the cost of accuracy. Figure 1 illustrates the limitations of current methods: while high accuracy often leads to

arXiv:2507.23599v3 [cs.CV] 28 Jan 2026

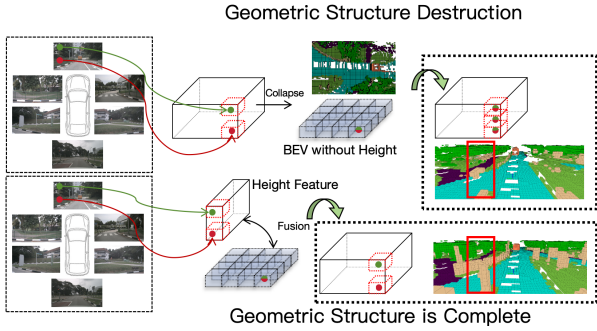


Figure 2: The top section illustrates traditional 2D BEV methods lead to the collapse of geometric structures, particularly in the vertical direction, during compression. The bottom section demonstrates how our approach effectively preserves these structures while maintaining efficiency, even in a purely 2D framework.

slower inference speeds, methods designed for faster inference tend to suffer significant accuracy loss, with performance differences exceeding 10%. This issue arises from the compression of vertical geometric structures, as shown in Figure 2. Methods relying solely on 2D BEV representations struggle to capture fine-grained spatial structures, which are essential for accurate scene understanding He et al. (2025); Li et al. (2025); Wu et al. (2024); Hou et al. (2024). The visualization results further emphasize the importance of preserving vertical geometric features to maintain the overall semantic and structural integrity of the 3D voxel space. Recent studies such as ProtoOcc Oh et al. (2025) preserve geometric completeness by directly extracting semantic cues from 3D voxel feature maps. And DHD proposed HeighNet Wu et al. (2024), which performs depth prediction at three fixed heights. However, these methods process all spatial dimensions uniformly, ignoring the strong imbalance in information density, particularly the fact that the vertical axis contains far fewer effective observations Zhang et al. (2024).

To preserve geometric integrity and accurately model the uneven information density across 3D space, we introduce a new representation strategy for processing voxel features. Specifically, we first slice the 3D voxel volume into height-aware 2D feature planes, which retain complete vertical structural information. Direction-Aware Convolution (DAC) is then employed to adaptively extract features along vertical and horizontal orientations, allocating computation to informative regions while suppressing redundancy in sparse dimensions. The resulting geometry-enhanced features are further fused with BEV representations to recover vertical cues that are typically lost in conventional BEV-based pipelines, leading to a more holistic 3D scene understanding.

In this work, we present DA-Occ, a Direction-Aware 3D Occupancy prediction framework that effectively captures geometric cues along both horizontal and vertical orientations. By preserving the full 3D voxel structure within a lightweight 2D processing pipeline, DA-Occ achieves high computational efficiency without sacrificing geometric integrity. On the Occ3D-nuScenes benchmark, DA-Occ achieves 39.3% mIoU at 27.7 FPS, striking a strong balance between accuracy and real-time inference, making it well suited for the deployment of au-

tonomous driving. Moreover, we report a combined accuracy–efficiency indicator as a supplementary metric, offering a concise way to quantify the balance between prediction quality and performance at runtime.

2. Related Work

2.1. 2D-to-3D View Transformation

Many existing methods utilize estimated depth information to project 2D image features into 3D voxel space Yan et al. (2023, 2025a,b); Wang et al. (2021); Yan et al. (2024). LSS Phillion and Fidler (2020) explicitly predicts depth distributions to lift 2D image features into 3D space. More recent approaches Li et al. (2023b,a); Miao et al. (2023) have highlighted the importance of accurate depth estimation in the view transformation process. For example, BEVDepth Li et al. (2023b) encodes both intrinsic and extrinsic camera parameters into its depth refinement module for improved 3D object detection. BEVStereo Li et al. (2023a) introduces an efficient temporal stereo mechanism to enhance depth estimation quality. In addition, some studies Zhang et al. (2023a); Xie et al. (2023); Huang and Huang (2022); Chi et al. (2023) focus on optimizing the projection stage itself. However, existing approaches have largely overlooked the potential of leveraging height prediction as a direct supervisory signal for view transformation. Unlike standard LSS-based lifting that relies solely on depth probability, we also incorporate height scores predicted from 2D images Wu et al. (2024) to explicitly guide the feature lifting process. This height-score projection provides a more accurate estimate of the vertical distribution within the voxel grid, enabling the model to retain fine-grained height information before BEV compression. As a result, the lifted voxel representation preserves vertical geometry more faithfully, offering a stronger foundation for subsequent BEV feature reconstruction.

2.2. 3D Occupancy Prediction

3D occupancy prediction reconstructs the 3D scene by predicting a dense voxel grid that encodes spatial occupancy He et al. (2025). A straightforward approach is to extend the BEV representation used in 3D object detection to the voxel space by lifting the BEV features to 3D Yu et al. (2023) and applying a segmentation head Huang et al. (2021); Li et al. (2023c); Hou et al. (2024); Park et al. (2025). However, this strategy disrupts the geometric integrity of the voxel representation due to the lack of vertical structure awareness. Directly processing full 3D voxel features, on the other hand, incurs substantial computational overhead. To address this, COTR Ma et al. (2024) introduces a compact voxel representation via down-sampling, while PanoOcc Wang et al. (2024) proposes a novel panoramic occupancy segmentation task and leverages sparse 3D convolutions to reduce computation. And ProtoOcc Oh et al. (2025) reconstructs 3D semantic information through a transformer-based framework that operates directly on voxel feature maps, achieving strong geometric completeness. Although ProtoOcc Oh et al. (2025), COTR Ma et al. (2024),

and PanoOcc Wang et al. (2024) preserve geometric structure within 3D voxels, they treat all spatial dimensions uniformly and do not account for the anisotropic data distribution inherent to camera-only perception Zhang et al. (2024). In contrast, our method explicitly exploits this imbalance through height-aware slicing and direction-aware convolution, allocating computation to informative regions while avoiding unnecessary overhead in sparse dimensions.

3. Method

In 3D occupancy prediction tasks, the surrounding environment is discretized into a voxel-based volumetric grid Phillion and Fidler (2020). We follow the standard occupancy coordinate convention, where X denotes the depth (forward) axis, Y the horizontal (left–right) axis, and Z the vertical (up–down) axis. Assuming the ego vehicle is located at the origin of the global coordinate system, the 3D perception range is defined by the bounds $[X_s, Y_s, Z_s, X_e, Y_e, Z_e]$, where $[X_s, Y_s, Z_s]$ and $[X_e, Y_e, Z_e]$ denote the lower and upper bounds along the depth, width, and height axes, respectively. The scene volume is partitioned into a grid of shape $[X, Y, Z]$ (e.g. $[200, 200, 1]$ as in Yu et al. (2023)). Accordingly, the physical size of a single voxel along each axis is computed as $[\frac{X_e-X_s}{X}, \frac{Y_e-Y_s}{Y}, \frac{Z_e-Z_s}{Z}]$. At inference time, each voxel is assigned a binary occupancy state—occupied or empty along with a semantic label from a predefined set of categories or an unknown class. The final voxel-wise predictions are derived from visual features extracted from multi-view images, denoted as $\mathbf{X} \in \mathbb{R}^{N \times C \times H \times W}$, where N is the number of cameras, $[C, H, W]$ is the feature size. Each camera is associated with both intrinsic and extrinsic parameters (K and $[R|t]$), which are utilized to transform 2D image features into the unified 3D coordinate space. These parameters enable precise projection and aggregation of multi-view information into the voxel grid for occupancy and semantic prediction.

3.1. Overall Architecture

The overall architecture of DA-Occ is depicted in detail in Figure 3. It comprises the following key components: (1) Image Backbone: A convolutional neural network (e.g., ResNet He et al. (2016)) is employed to extract high-level visual features from multi-view input images. (2) Direction-Aware Geometric Encoder (DGE): This module integrates a depth estimation network (DepthNet) and a height-aware estimation network (HeightNet) to jointly capture geometric cues along both horizontal and vertical directions. By leveraging direction-aware feature extraction, DGE enriches the voxel representation with accurate geometric structure, providing a more reliable foundation for subsequent 3D occupancy reasoning. (3) 2D-to-3D View Transformation: Image-plane features are lifted into the 3D voxel space using calibrated projection matrices, enabling spatial alignment across multiple views. (4) Direction-Aware Geometric Decoder (DGD): The final decoding stage incorporates geometric priors to enhance 3D structural consistency and improve the granularity of semantic predictions within the voxel grid.

3.2. Direction-Aware 2D Convolution

To maintain the consistency of 3D geometric structures and account for the non-uniform data density across different spatial directions, particularly along the vertical axis, we introduce the Direction-Aware 2D Convolution. This operation is utilized in both the Direction-Aware Geometric Encoder and the Direction-Aware Geometric Decoder, but at different stages of the model pipeline. Within the encoder, Direction-Aware Convolution is applied prior to the 2D-to-3D view transformation to dynamically predict height scores, thereby enriching the vertical geometric representation. Additionally, by adapting to the naturally sparse distribution of camera-based observations along the height axis, it avoids overfitting and maintains stable feature learning. After the transformation, Direction-Aware Convolution is used in the decoder to refine and restore geometric structures along vertical and horizontal axes, enabling a more complete and structurally accurate 3D representation.

Inspired by ParC-Net Zhang et al. (2022), which captures long-range dependencies in 2D image space, we propose a novel extension of this mechanism to the 3D voxel domain. Our extension dynamically extracts 3D geometric features, enabling the model to better capture long-range spatial dependencies and enhance the representation of 3D structures. By introducing Direction-Aware Convolution that model dependencies along both the vertical and horizontal axes, our approach preserves fine-grained 3D structure within a purely 2D framework.

To preserve fine-grained geometric structure along different spatial axes, we introduce a Direction-Aware Convolution (DAC), denoted as $\mathcal{D}_{dir}(\cdot)$, where $dir \in \{h, v\}$ corresponds to the horizontal and vertical directions in feature map, respectively. Given an input feature map $\mathbf{F}_{in} \in \mathbb{R}^{C \times H \times W}$, the computation proceeds in three steps:

$$\begin{aligned} W_{dir} &= g(\mathcal{P}_{dir}(\mathbf{F}_{in})), \\ \mathbf{F}_{mid}^{dir} &= \mathbf{F}_{in} \oplus \mathbf{F}_{shift}^{dir}, \\ \mathbf{F}_{out} &= \mathcal{C}_{dir}(\mathbf{F}_{mid}^{dir} + p_{dir}; W_{dir}). \end{aligned} \quad (1)$$

Here: - $\mathcal{P}_{dir}(\cdot)$ is a directional average pooling operator (row-wise for v , column-wise for h). - $g(\cdot)$ is an MLP that generates dynamic convolution weights W_{dir} . - \oplus denotes channel-wise concatenation. - \mathbf{F}_{shift}^{dir} represents direction-specific shifted features:

$$\mathbf{F}_{shift}^v = \mathbf{F}_{in}[:, :, :H-1, :], \quad \mathbf{F}_{shift}^h = \mathbf{F}_{in}[:, :, :, :W-1].$$

- p_{dir} is a learnable positional encoding ($H \times 1$ for vertical, $1 \times W$ for horizontal). - $\mathcal{C}_{dir}(\cdot)$ denotes a convolution whose kernel weights are determined by W_{dir} . This formulation allows DAC to adaptively emphasize geometric structures along different orientations, enabling fine-grained vertical and horizontal feature extraction while maintaining lightweight computational cost.

3.3. Direction-Aware Geometric Encoder

Height estimation network (HeightNet) first introduced in DHD Wu et al. (2024), shares a similar structure with the DepthNet in BEVDepth Li et al. (2023b). It is used to generate

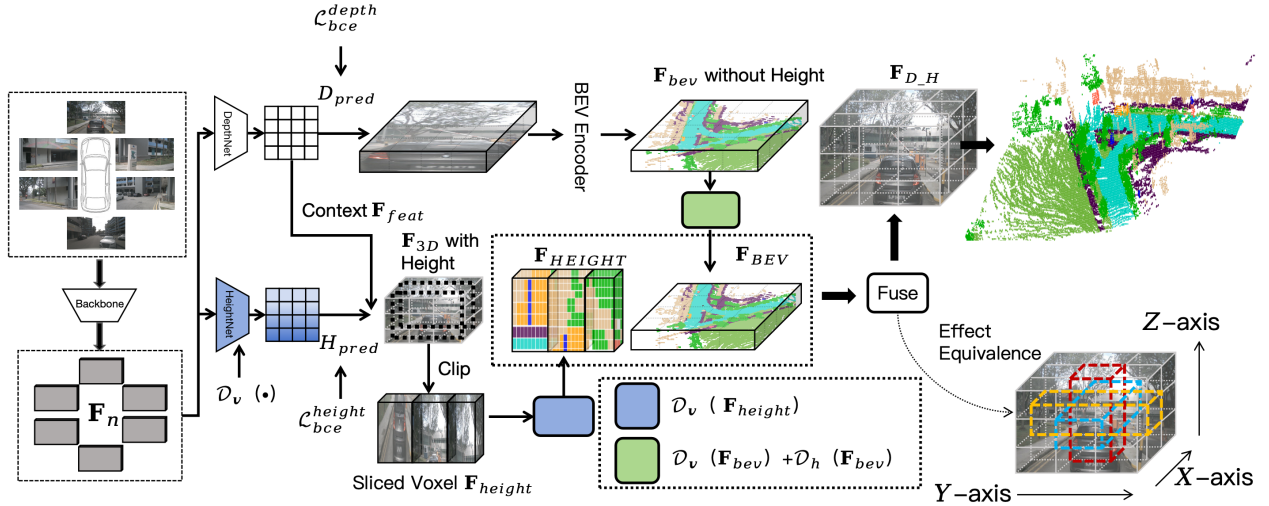


Figure 3: This diagram illustrates the overall architecture of DA-Occ. The left side shows the input images processed by the Backbone, generating feature maps \mathbf{F}_n that are fed into the DepthNet and HeightNet for depth and height predictions. These features are then used to construct 3D features \mathbf{F}_{3D} (with height) and BEV features \mathbf{F}_{bev} (without height). The DAC ($\mathcal{D}_v(\cdot)$ and $\mathcal{D}_h(\cdot)$) are applied to enhance the feature representation. Finally, these features are fused to produce the final output, which is visualized on the right side. (To facilitate understanding, some feature maps use the original images instead.)

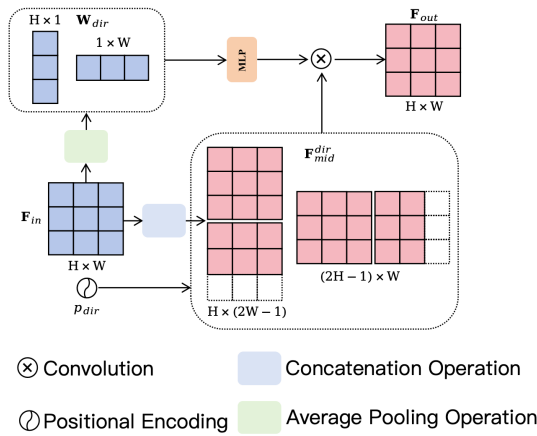


Figure 4: Internal operations of Direction-Aware 2D Convolution. This process first performs directional average value compression on the input feature \mathbf{F}_{in} (in the horizontal or vertical direction) to generate one of \mathbf{F}_h or \mathbf{F}_v . This intermediate result is passed through a Multi-Layer Perceptron (MLP) to generate dynamic convolutional weights. These weights are then applied to a concatenated feature tensor via convolution, producing the final output feature \mathbf{F}_{out} .

a predicted height map H_{pred} , which is supervised by a ground-truth height map H_{gt} to facilitate accurate height estimation. The generation of H_{gt} proceeds as follows: a LiDAR point $p_l = [x_l, y_l, z_l, 1]^T$ in the LiDAR coordinate frame is transformed to the ego-vehicle coordinate system as $p_e = [x_e, y_e, z_e, 1]^T$. The corresponding 2D projection onto the image plane is computed using:

$$d[u, v, 1]^T = K[R|t][x_l, y_l, z_l, 1]^T \quad (2)$$

where d is the depth value in the camera coordinate system, $[u, v, 1]$ denotes the pixel coordinates in homogeneous form, K is the intrinsic matrix, and $R \in \mathbb{R}^{3 \times 3}$, $t \in \mathbb{R}^3$ are the camera extrinsic parameters.

Following Wu et al. (2024), we construct a set of tuples

$[u, v, d, z_e]^T$, where each pixel location $[u, v]$ is assigned both a projected depth d and a corresponding height z_e in the ego coordinate system. For each pixel, only the point with the smallest depth is retained to eliminate occluded redundancies, resulting in a ground-truth height map H_{gt} that represents the visible uppermost surface in the scene.

Height-aware estimation network is designed to predict H_{pred} by leveraging structural priors along the vertical (Z-axis) direction. While DHD applies height scores to perform three separate projections over fixed height ranges, our approach uses the predicted height distribution to directly produce height-aware 3D voxel features. This design avoids the limitations of discretized height bins and allows the model to adaptively preserve vertical structure with finer granularity.

HeightNet incorporates both the geometric shape prior of objects in height and the contextual information from adjacent horizontal locations. To better capture the vertical geometric structure while keeping the module lightweight, we replace the last two 3×3 convolutional blocks in DepthNet with two vertical Direction-Aware Convolution operations $\mathcal{D}_v(\cdot)$. This architectural modification enables more effective extraction of height-sensitive features with minimal additional cost.

The entire Direction-Aware Geometric Encoder process is described as follows: \mathbf{F}_n is processed by DepthNet, generating the depth score D_{pred} and the feature map \mathbf{F}_{feat} . \mathbf{F}_n is parallel passed through HeightNet, producing the height score H_{pred} .

3.4. 2D-to-3D View Transformation

To preserve the integrity of 3D geometric structures while maintaining computational efficiency, we adopt the Lift-Splat-Shoot (LSS) framework Phillion and Fidler (2020) for view transformation. Unlike existing approaches such as FlashOcc Yu et al. (2023), which rely on a purely 2D transformation grid (e.g., $1 \times 200 \times 200$) and often compress the vertical dimension, resulting in significant geometric distortion,

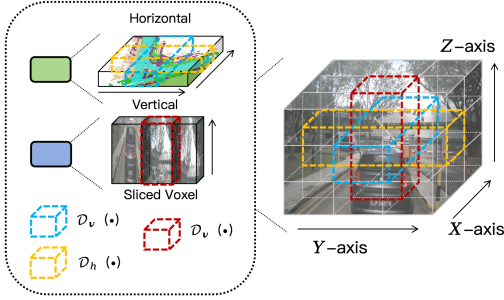


Figure 5: It illustrates the combined effects of \mathcal{D}_v in \mathbf{F}_{height} , and \mathcal{D}_v and \mathcal{D}_h in \mathbf{F}_{bev} . The right side presents an equivalent depiction of these effects, highlighting the collaborative extraction of geometric features along the X, Y, and Z axes, and emphasizing the synergy between the three axes in capturing spatial information.

our method takes a different approach. We adopt a lightweight 3D voxel grid (e.g., $16 \times 32 \times 32$) to enrich the BEV feature map with enhanced vertical geometric information. This enables BEV feature map to retain vertical spatial cues more effectively and recover structural geometry with higher fidelity under similar computational constraints.

Specifically, we construct a 3D voxel grid that enables finer-grained depth and height modeling during the lifting process. The generated 3D voxel features are then sliced and fused along the depth axis (X-axis), effectively capturing vertical structure while still allowing the final output to remain in a 2D feature map format for efficient processing. In the Splat stage of the LSS, we enhance the lifted 3D voxel representation by the predicted height confidence scores. Specifically, the resulting voxel projection is formulated as:

$$\mathbf{F}_{3D} = \sum_{i \in \text{ranks_bev}[z]=v} \text{softmax}(H_{pred}) \cdot \mathbf{F}_{feat,i} \quad (3)$$

where $\text{softmax}(\cdot)$ is applied along Z for each (x, y) location on $H_{pred} \in \mathbb{R}^{B \times Z \times X \times Y}$, and $\mathbf{F}_{feat,i}$ from DepthNet represents the i -th pixel feature. This design enhances the model’s perception of vertical geometric structures while maintaining real-time inference efficiency, leading to improved spatial feature representation. After constructing the 3D voxel feature volume $\mathbf{F}_{3D} \in \mathbb{R}^{B \times C \times Z \times X \times Y}$, we perform slicing along the depth axis (i.e., the X-axis) and concatenate the resulting slices along the horizontal axis (Y-axis). This transforms the 3D voxel structure into a 2D feature map with enhanced perception of vertical (height-wise) geometric structures, facilitating more efficient extraction of height-aware spatial representations. This process is described as:

$$\mathbf{F}_{height} = \text{Cat}_{k=0}^{k=X-1}(\mathbf{F}_{3D}[:, :, :, k, :], \text{dim} = 4) \quad (4)$$

where the concatenation is applied along the spatial Y-axis, resulting in a feature map $\mathbf{F}_{height} \in \mathbb{R}^{B \times C \times Z \times (X \times Y)}$

3.5. Direction-Aware Geometric Decoder

The BEV feature map \mathbf{F}_{bev} , which primarily encodes the target’s depth-related information, and the sliced height-aware

feature map \mathbf{F}_{height} , which captures the target’s vertical structural cues, are obtained following the view transformation stage. The \mathbf{F}_{bev} captures the relative distance between the ego vehicle and the surrounding targets. This spatial relationship can be further decomposed into *front-back* and *left-right* directional components within the BEV plane. To better model depth-related geometric structures, we apply a directional attention operator $\mathcal{D}_{dir}(\cdot)$ on the X and Y axes of the BEV feature map. The refined BEV representation is computed as:

$$\mathbf{F}_{BEV} = \mathcal{D}_h(\mathbf{F}_{bev}) + \mathcal{D}_v(\mathbf{F}_{bev}) \quad (5)$$

where the output \mathbf{F}_{BEV} has the same shape as the input \mathbf{F}_{bev} , and the fusion enhances geometric sensitivity in both planar directions.

Due to the previous processing of the sliced \mathbf{F}_{height} , it preserves the geometric structure in the vertical direction. The \mathcal{D}_v aligns better with the vertical structure. This directional sensitivity allows it to capture and refine height-dependent geometric features more effectively. The refinement process is defined as:

$$\mathbf{F}_{HEIGHT} = \text{Cat}_{z=0}^{z=Z-1}(\mathcal{D}_v(\mathbf{F}_{height})[:, :, z], \text{dim} = 1) \quad (6)$$

where $\mathbf{F}_{height} \in \mathbb{R}^{B \times C \times Z \times (Y \cdot X)}$, and $\mathbf{F}_{HEIGHT} \in \mathbb{R}^{B \times (C \cdot Z) \times Y \times X}$ is obtained by concatenating the Z-axis slices along the channel dimension and then reshaping the last axis from $Y \cdot X$ to (Y, X) .

This formulation allows for the fine-grained recovery of vertical geometric structures and enhances the spatiotemporal expressiveness of height features. The final representation of characteristics, $\mathbf{F}_{D,H}$, is obtained by merging \mathbf{F}_{HEIGHT} and \mathbf{F}_{BEV} , effectively combining fine-grained height-based information with depth-based information to improve understanding of 3D space. The fusion process is carried out by concatenating \mathbf{F}_{HEIGHT} and \mathbf{F}_{BEV} along the channel dimension, followed by a point convolution operation. The effect of $\mathcal{D}_h(\cdot)$ and $\mathcal{D}_v(\cdot)$ on the feature of BEV is illustrated in Figure 5.

4. Experiment

4.1. Dataset and Evaluation Metrics

We train and evaluate our model on the Occ3D-nuScenes benchmark Tian et al. (2023), which is built upon the nuScenes dataset Caesar et al. (2020). The dataset comprises 1,000 video sequences, split into 700 for training, 150 for validation, and 150 for testing. Each keyframe includes a 32-beam LiDAR point cloud, six RGB images from surround-view cameras, and dense voxel-level semantic occupancy annotations. The perception range is defined as $[-40 \text{ m}, -40 \text{ m}, -1 \text{ m}, 40 \text{ m}, 40 \text{ m}, 5.4 \text{ m}]$, and the voxel resolution is set to $[0.4 \text{ m}, 0.4 \text{ m}, 0.4 \text{ m}]$. Each voxel is assigned one of 18 semantic classes, including 16 predefined object categories, one *other* class for unknown objects, and one *empty* class representing free space. To assess the performance of our approach, we adopt evaluation metrics widely used in 3D occupancy prediction: the mean Intersection-over-Union (mIoU) Liu et al. (2024), computed over all semantic categories.

4.2. Implementation Details

Following common practice Ma et al. (2024); Li et al. (2023c); Liu et al. (2024), we train our models using 4 NVIDIA H800 GPUs with a batch size of 4 per GPU. Unless otherwise specified, all models are optimized using the AdamW optimizer with a learning rate of 1×10^{-4} and a weight decay of 0.05. During the LSS stage, the resolution of the grid for the depth score is set to $[1 \times 200 \times 200]$, and the resolution of the grid for the height score is set to $[16 \times 32 \times 32]$. Regarding the loss function, we design it based on the characteristics of geometric structure recovery in DA-Occ. Specifically, we follow the formulation proposed in MonoScene Cao and De Charette (2022) and define the overall loss as: $\mathcal{L} = \lambda_1 \mathcal{L}_{\text{bce}}^{\text{depth}} + \lambda_2 \mathcal{L}_{\text{bce}}^{\text{height}} + \lambda_3 \mathcal{L}_{\text{ce}} + \lambda_4 \mathcal{L}_{\text{scal}}^{\text{sem}} + \lambda_5 \mathcal{L}_{\text{scal}}^{\text{geo}}$, where $\lambda_1, \lambda_2, \lambda_3, \lambda_4, \lambda_5$ are set as 1.0, 1.0, 10.0, 1.0, 1.0. For inference, we use a single NVIDIA A100 GPU with a batch size of 1. The frame-per-second (FPS) metric is measured using the official mmdetection3d codebase.

4.3. Main Results

Since occupancy prediction models are ultimately deployed in real-time autonomous driving systems, accuracy alone cannot reflect their practical utility. In addition to standard mIoU and FPS, we therefore report a family of real-time-normalized metrics, denoted as RT-mIoU@K:

$$\text{RT-mIoU@K} = \text{mIoU} \times \min\left(\frac{\text{FPS}}{K}, 1\right)$$

where FPS is the measured inference speed and K is a target frame rate. When $\text{FPS} < K$, the metric linearly penalizes slow models; when $\text{FPS} \geq K$, RT-mIoU@K reduces to the original mIoU, reflecting the practical view that exceeding the required frame rate does not further improve safety.

In our experiments we report RT-mIoU@10, RT-mIoU@15, and RT-mIoU@20. Following prior work Yu et al. (2023); Hou et al. (2024), $K = 10$ corresponds to a relaxed real-time requirement. However, this level can be insufficient in high-speed scenarios. For example, at a highway speed of 120 km/h (≈ 33.3 m/s), 10 FPS produces predictions every 100 ms, during which the ego vehicle travels about 3.33 m and may enter a substantially different spatial configuration between frames. In contrast, 20 FPS reduces the inter-frame displacement to 1.67 m at the same speed, providing a stricter safety margin. We therefore treat RT-mIoU@10 as a lenient setting and RT-mIoU@15/@20 as progressively stricter, safety-critical regimes.

As shown in Table 1, DA-Occ consistently achieves the highest RT-mIoU@K across all $K \in \{10, 15, 20\}$, indicating a superior balance between accuracy and efficiency under different real-time requirements.

Table 1 presents a comparison between DA-Occ and state-of-the-art (SOTA) methods on the Occ3D-nuScenes benchmark. The results are grouped by the number of frames used in the temporal sequence. DA-Occ demonstrates outstanding efficiency while maintaining high accuracy. Notably, even when using only a single frame for data fusion, DA-Occ* achieves accuracy comparable to that of many multi-frame models. This is largely attributed to the use of the Stereo4D strategy in its

temporal fusion module Huang et al. (2021). When using a single frame, the proposed method improves accuracy by 2.43% compared to FlashOcc. By employing the frame fusion technique at the BEV level Liu et al. (2024), DA-Occ achieves FPS of 27.7 and accuracy of 39.3%. These results highlight DA-Occ’s ability to strike an effective balance between efficiency and accuracy.

It is important to note that, like FlashOcc, DA-Occ does not use depth supervision when temporal fusion is not applied. The way we make comparisons is based on innovations within the model itself, including models such as MonoScene Cao and De Charette (2022), TPVFormer Huang et al. (2023), CTF-Occ Ma et al. (2024), OccFormer Zhang et al. (2023b), BEVDetOcc Huang et al. (2021), FlashOcc Yu et al. (2023), FB-OCC Li et al. (2023c), GSD-Occ He et al. (2025), EOPIA Park et al. (2025), and COTR Ma et al. (2024) (since the model does not have a specific name, the abbreviation of the article title is used instead). These results underscore the effectiveness of DA-Occ in preserving geometric structures using a purely 2D-based approach. To further validate this capability, we conduct both ablation studies and qualitative visualizations, which consistently confirm the robustness of DA-Occ in maintaining geometric structural integrity.

4.4. Ablation Studies

To accelerate experimental evaluation, we conducted ablation experiments on the model by removing both DepthNet and temporal fusion. To investigate the impact of height information on occupancy prediction, we varied the resolution of the 3D voxel grid and analyzed how vertical geometric granularity influences performance. The impact of the X and Y grid sizes on accuracy is negligible, as these dimensions primarily encode depth information, which is predominantly derived from the BEV feature map. The results, summarized in Table 2, highlight the crucial role of height-aware geometry in achieving accurate 3D occupancy predictions.

Next, to assess the effectiveness of DAC in preserving geometric structures, we performed additional ablation studies on the nuScenes dataset, as shown in Table 3. The results confirm DAC are highly effective at capturing structural features, contributing to both improved performance and model efficiency.

To further evaluate the robustness of DA-Occ, we conducted experiments without using the Visible Mask. This setting simulates real-world scenarios where the model may not have access to complete or perfect information, enabling us to evaluate the model’s ability to generalize and maintain accuracy under challenging conditions. The results, presented in Table 4, demonstrate that DA-Occ achieves an mIoU of 31.31% without the Visible Mask, indicating its strong resilience to missing data and its robustness in less-than-ideal environments.

Finally, we simulated the inference speed of DA-Occ on edge devices by imposing several hardware constraints to mimic real-world deployment environments. Specifically, we limited the available GPU memory to 4GB (with other memory occupied to simulate concurrent tasks on the edge device) and restricted the GPU’s maximum power consumption to 90W. As

Table 1: Comparison with state-of-the-art methods on the Occ3D-nuScenes benchmark. FPS is tested on a single NVIDIA A100 using the mmdetection3d codebase. DA-Occ* and FlashOcc* represent the way of Stereo4D temporal fusion Huang et al. (2021), the 16-frame fusion method adopts the BEV-level approach Liu et al. (2024).

Method	Venue	History Frames	Backbone	Image Size	mIoU (%)	FPS	RT-mIoU@10/@15/@20
MonoScene	CVPR'22	-	ResNet-101	928×1600	6.06	1.2	0.73/0.48/0.36
TPVFormer	CVPR'23	-	ResNet-101	928×1600	27.83	3.1	8.63/5.75/4.31
CTF-Occ	NIPS'24	-	ResNet-101	928×1600	28.53	-	-
OccFormer	ICCV'23	-	ResNet-50	256×704	20.40	-	-
BEVDetOcc	arXiv'22	-	ResNet-50	256×704	31.64	-	-
FlashOcc	arXiv'23	-	ResNet-50	256×704	31.95	79.4	31.95/31.95/31.95
ProtoOcc	CVPR'25	-	ResNet-50	432×800	37.80	9.6	36.29/24.19/18.14
DHD	ICRA'25	-	ResNet-50	256×704	36.50	9.5	34.68/23.12/17.34
DA-Occ(Ours)	-	-	ResNet-50	256×704	34.38	39.6	34.38/ 34.38/34.38
BEVDetOcc-4D-Stereo	arXiv'22	1	ResNet-50	256×704	36.01	1.8	6.48/4.32/3.24
FB-OCC	ICCV'23	1	ResNet-50	256×704	37.52	6.9	25.89/17.26/12.94
FlashOCC*	arXiv'23	1	ResNet-50	256×704	37.84	9.1	34.43/22.96/17.22
GSD-Occ	AAAI'25	1	ResNet-50	256×704	34.84	22.7	34.84/34.84/34.84
EOPIA	ICAIIC'25	1	ResNet-50	256×704	35.26	28.7	35.26/35.26/35.26
DA-Occ(Ours)*	-	1	ResNet-50	256×704	38.97	7.3	28.45/18.97/14.22
DA-Occ(Ours)	-	1	ResNet-50	256×704	35.77	31.5	35.77/35.77/35.77
FastOCC	ICRA'24	16	ResNet-101	320×800	37.2	10.1	37.2/25.05/18.79
COTR	CVPR'24	16	ResNet-50	256×704	44.5	0.9	4.01/2.67/2.01
GSD-Occ	AAAI'25	16	ResNet-50	256×704	39.4	20.0	39.40/39.40/39.40
DA-Occ(Ours)	-	16	ResNet-50	256×704	39.3	27.7	39.30/39.30/39.30

Table 2: Effect of voxel grid resolution on mIoU, inference speed, and FLOPs.

Size of Grid	mIoU (%)	FPS	GFLOPs
16 × 32 × 32	34.38	39.6	276.59
16 × 64 × 64	34.45	38.7	276.65
8 × 32 × 32	33.67	38.9	276.58
4 × 32 × 32	32.89	40.1	276.55

Table 3: Effect of DAC in HeightNet and in BEV on mIoU, inference speed, and FLOPs.

HeightNet	BEV	mIoU (%)	FPS	Flops
✓	✓	34.38	39.6	276.59G
✓	-	34.01	42.5	271.24G
-	✓	33.76	41.3	276.57G
-	-	32.58	44.7	271.21G

shown in Table 5, even under these simulated deployment constraints, DA-Occ maintains its effectiveness. This further validates the applicability of DA-Occ for real-time inference on edge devices.

4.5. Visualization Studies

In visualization experiments, we adopt FlashOcc Yu et al. (2023) as the benchmark model, including both non-temporal variants and deeply supervised versions for comparison. A variety of scenarios from the val set are employed to ensure comprehensive evaluation. All visualizations are generated using

Table 4: The mIoU and FPS of each model without the visible mask.

Method	Venue	mIoU (%)	FPS
MonoScene	CVPR'22	6.06	1.2
OccFormer	ICCV'23	20.40	-
CTF-Occ	NIPS'24	28.53	-
BEVDet	arXiv'22	18.05	-
SparseOcc	ECCV'24	30.64	17.7
DA-Occ	-	31.31	27.7

Table 5: Model inference speed of simulated edge device.

Precision	Threads	GPU Memory	FPS
FP32 (A100)	Full	Full	39.6
FP16 (A100)	2	4GB	14.8

the official FlashOcc codebase. As shown in Figure 6, the red box highlights a significant semantic loss along the vertical axis in FlashOcc. In contrast, DA-Occ maintains geometric structures in both horizontal and vertical directions, even within a purely 2D framework. This structural consistency greatly contributes to its outstanding mIoU performance.

5. Discussion and Limitations

This work introduces DA-Occ, a 2D-based framework for efficient and geometrically consistent 3D occupancy prediction. By combining height-aware voxel slicing with a direction-

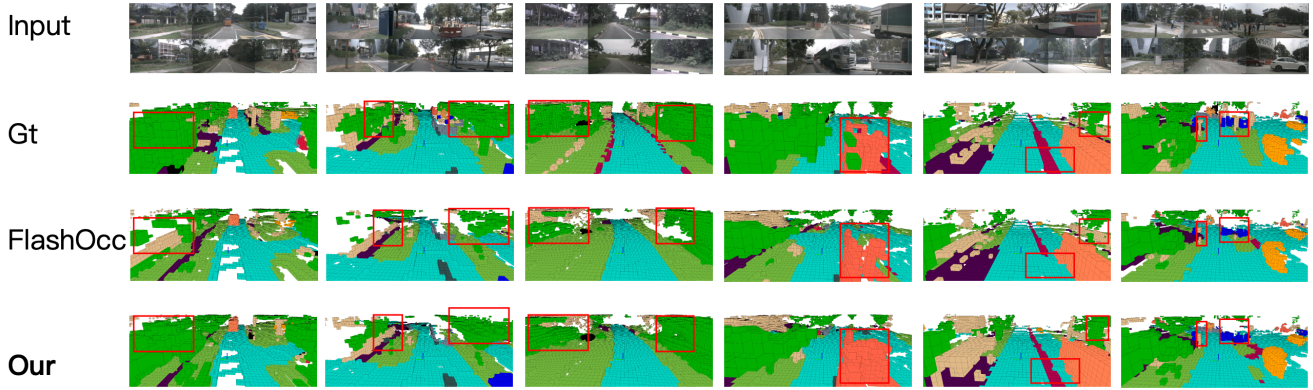


Figure 6: This figure shows the comparison of the proposed method with FlashOcc in the visualization experiments. Our method demonstrates better generalization of geometric structures, resulting in more accurate segmentation in challenging areas.

aware convolution (DAC) module, the framework preserves vertical structure that is typically suppressed in conventional bird’s-eye-view pipelines, while keeping the computational cost low. From an autonomous driving perspective, this design enables the perception stack to maintain reliable occupancy estimates even at high vehicle speeds and under tight latency budgets. Experiments on the Occ3D-nuScenes benchmark demonstrate that DA-Occ achieves a favorable balance between accuracy and runtime, and delivers stronger real-time performance than existing alternatives. These results indicate that DA-Occ can improve geometric fidelity in scene understanding and is a practical candidate for deployment in autonomous driving systems operating under strict real-time constraints. Several limitations of the present study point to directions for future work. First, the empirical evaluation is conducted on a single dataset and under limited weather and illumination conditions. A more comprehensive assessment should include cross-domain scenarios such as diverse urban layouts, adverse weather (e.g., rain, fog, snow), and nighttime driving. To improve robustness in these settings, we plan to explore self-supervised pre-training, domain adaptation, and style-transfer-based data augmentation, with the goal of learning occupancy predictors that generalize across large-scale, multi-source data.

Acknowledgments

This work was supported by the Nanjing Desay SV Automotive co.,LTD. under Grant Nos. TRD2025001.

References

Arnold, E., Al-Jarrah, O.Y., Dianati, M., Fallah, S., Oxtoby, D., Mouzakitis, A., 2019. A survey on 3d object detection methods for autonomous driving applications. *IEEE Transactions on Intelligent Transportation Systems* 20, 3782–3795.

Caesar, H., Bankiti, V., Lang, A.H., Vora, S., Liong, V.E., Xu, Q., Krishnan, A., Pan, Y., Baldan, G., Beijbom, O., 2020. nuscenes: A multimodal dataset for autonomous driving, in: *Proceedings of the IEEE/CVF conference on computer vision and pattern recognition*, pp. 11621–11631.

Cao, A.Q., De Charette, R., 2022. Monoscene: Monocular 3d semantic scene completion, in: *Proceedings of the IEEE/CVF Conference on Computer Vision and Pattern Recognition*, pp. 3991–4001.

Chi, X., Liu, J., Lu, M., Zhang, R., Wang, Z., Guo, Y., Zhang, S., 2023. Bev-san: Accurate bev 3d object detection via slice attention networks, in: *Proceedings of the IEEE/CVF Conference on Computer Vision and Pattern Recognition*, pp. 17461–17470.

He, K., Zhang, X., Ren, S., Sun, J., 2016. Deep residual learning for image recognition, in: *Proceedings of the IEEE conference on computer vision and pattern recognition*, pp. 770–778.

He, Y., Chen, W., Wang, S., Xun, T., Tan, Y., 2025. Achieving speed-accuracy balance in vision-based 3d occupancy prediction via geometric-semantic disentanglement, in: *Proceedings of the AAAI Conference on Artificial Intelligence*, pp. 3455–3463.

Hou, J., Li, X., Guan, W., Zhang, G., Feng, D., Du, Y., Xue, X., Pu, J., 2024. Fastocc: Accelerating 3d occupancy prediction by fusing the 2d bird’s-eye view and perspective view, in: *2024 IEEE International Conference on Robotics and Automation (ICRA)*, IEEE. pp. 16425–16431.

Huang, J., Huang, G., 2022. Bevpoolv2: A cutting-edge implementation of bevdet toward deployment. *arXiv preprint arXiv:2211.17111*.

Huang, J., Huang, G., Zhu, Z., Ye, Y., Du, D., 2021. Bevdet: High-performance multi-camera 3d object detection in bird-eye-view. *arXiv preprint arXiv:2112.11790*.

Huang, Y., Zheng, W., Zhang, Y., Zhou, J., Lu, J., 2023. Tri-perspective view for vision-based 3d semantic occupancy prediction, in: *Proceedings of the IEEE/CVF conference on computer vision and pattern recognition*, pp. 9223–9232.

Li, F., Xu, K., Wang, Z., Cui, Y., Billah, M.M., Liu, J., 2025. Instancebev: Unifying instance and bev representation for global modeling. *arXiv preprint arXiv:2505.13817*.

- Li, Y., Bao, H., Ge, Z., Yang, J., Sun, J., Li, Z., 2023a. Bevestereo: Enhancing depth estimation in multi-view 3d object detection with temporal stereo, in: Proceedings of the AAAI Conference on Artificial Intelligence, pp. 1486–1494.
- Li, Y., Ge, Z., Yu, G., Yang, J., Wang, Z., Shi, Y., Sun, J., Li, Z., 2023b. Bevdepth: Acquisition of reliable depth for multi-view 3d object detection, in: Proceedings of the AAAI conference on artificial intelligence, pp. 1477–1485.
- Li, Z., Yu, Z., Wang, W., Anandkumar, A., Lu, T., Alvarez, J.M., 2023c. Fb-bev: Bev representation from forward-backward view transformations, in: Proceedings of the IEEE/CVF International Conference on Computer Vision, pp. 6919–6928.
- Liang, T., Xie, H., Yu, K., Xia, Z., Lin, Z., Wang, Y., Tang, T., Wang, B., Tang, Z., 2022. Bevfusion: A simple and robust lidar-camera fusion framework. *Advances in Neural Information Processing Systems* 35, 10421–10434.
- Liu, H., Chen, Y., Wang, H., Yang, Z., Li, T., Zeng, J., Chen, L., Li, H., Wang, L., 2024. Fully sparse 3d occupancy prediction, in: European Conference on Computer Vision, Springer. pp. 54–71.
- Ma, Q., Tan, X., Qu, Y., Ma, L., Zhang, Z., Xie, Y., 2024. Cotr: Compact occupancy transformer for vision-based 3d occupancy prediction, in: Proceedings of the IEEE/CVF Conference on Computer Vision and Pattern Recognition, pp. 19936–19945.
- Miao, R., Liu, W., Chen, M., Gong, Z., Xu, W., Hu, C., Zhou, S., 2023. Occdepth: A depth-aware method for 3d semantic scene completion. *arXiv preprint arXiv:2302.13540*.
- Oh, G., Kim, S., Ko, H., Chi, H.g., Kim, J., Lee, D., Ji, D., Choi, S., Jang, S., Kim, S., 2025. 3d occupancy prediction with low-resolution queries via prototype-aware view transformation, in: Proceedings of the Computer Vision and Pattern Recognition Conference, pp. 17134–17144.
- Park, S., Song, J., Hwang, S., 2025. Efficient occupancy prediction with instance-level attention, in: 2025 International Conference on Artificial Intelligence in Information and Communication (ICAIIIC), IEEE. pp. 0103–0107.
- Phillion, J., Fidler, S., 2020. Lift, splat, shoot: Encoding images from arbitrary camera rigs by implicitly unprojecting to 3d, in: *Computer Vision—ECCV 2020: 16th European Conference, Glasgow, UK, August 23–28, 2020, Proceedings, Part XIV* 16, Springer. pp. 194–210.
- Tian, X., Jiang, T., Yun, L., Mao, Y., Yang, H., Wang, Y., Wang, Y., Zhao, H., 2023. Occ3d: A large-scale 3d occupancy prediction benchmark for autonomous driving. *Advances in Neural Information Processing Systems* 36, 64318–64330.
- Wang, K., Zhang, Z., Yan, Z., Li, X., Xu, B., Li, J., Yang, J., 2021. Regularizing nighttime weirdness: Efficient self-supervised monocular depth estimation in the dark, in: Proceedings of the IEEE/CVF international conference on computer vision, pp. 16055–16064.
- Wang, Y., Chen, Y., Liao, X., Fan, L., Zhang, Z., 2024. Panoocc: Unified occupancy representation for camera-based 3d panoptic segmentation, in: Proceedings of the IEEE/CVF conference on computer vision and pattern recognition, pp. 17158–17168.
- Wei, Y., Zhao, L., Zheng, W., Zhu, Z., Zhou, J., Lu, J., 2023. Surroundocc: Multi-camera 3d occupancy prediction for autonomous driving, in: Proceedings of the IEEE/CVF International Conference on Computer Vision, pp. 21729–21740.
- Wu, Y., Yan, Z., Wang, Z., Li, X., Hui, L., Yang, J., 2024. Deep height decoupling for precise vision-based 3d occupancy prediction. *arXiv preprint arXiv:2409.07972*.
- Xie, Y., Xu, C., Rakotosaona, M.J., Rim, P., Tombari, F., Keutzer, K., Tomizuka, M., Zhan, W., 2023. Sparsefusion: Fusing multi-modal sparse representations for multi-sensor 3d object detection, in: Proceedings of the IEEE/CVF International Conference on Computer Vision, pp. 17591–17602.
- Yan, Z., Li, X., Hui, L., Zhang, Z., Li, J., Yang, J., 2025a. Rignet++: Semantic assisted repetitive image guided network for depth completion: Z. yan et al. *International Journal of Computer Vision*, 1–23.
- Yan, Z., Wang, K., Li, X., Zhang, Z., Li, J., Yang, J., 2023. Desnet: Decomposed scale-consistent network for unsupervised depth completion, in: Proceedings of the AAAI conference on artificial intelligence, pp. 3109–3117.
- Yan, Z., Wang, Z., Wang, K., Li, J., Yang, J., 2025b. Completion as enhancement: A degradation-aware selective image guided network for depth completion, in: Proceedings of the Computer Vision and Pattern Recognition Conference, pp. 26943–26953.
- Yan, Z., Zheng, Y., Fan, D.P., Li, X., Li, J., Yang, J., 2024. Learnable differencing center for nighttime depth perception. *Visual Intelligence* 2, 15.
- Yin, T., Zhou, X., Krahenbuhl, P., 2021. Center-based 3d object detection and tracking, in: Proceedings of the IEEE/CVF conference on computer vision and pattern recognition, pp. 11784–11793.
- Yu, Z., Shu, C., Deng, J., Lu, K., Liu, Z., Yu, J., Yang, D., Li, H., Chen, Y., 2023. Flashocc: Fast and memory-efficient occupancy prediction via channel-to-height plugin. *arXiv preprint arXiv:2311.12058*.
- Zhang, H., Hu, W., Wang, X., 2022. Parc-net: Position aware circular convolution with merits from convnets and transformer, in: European conference on computer vision, Springer. pp. 613–630.

- Zhang, J., Zhang, Y., Liu, Q., Wang, Y., 2023a. Sa-bev: Generating semantic-aware bird's-eye-view feature for multi-view 3d object detection, in: Proceedings of the IEEE/CVF International Conference on Computer Vision, pp. 3348–3357.
- Zhang, J., Zhang, Y., Liu, Q., Wang, Y., 2024. Lightweight spatial embedding for vision-based 3d occupancy prediction. arXiv preprint arXiv:2412.05976 .
- Zhang, Y., Zhu, Z., Du, D., 2023b. Occformer: Dual-path transformer for vision-based 3d semantic occupancy prediction, in: Proceedings of the IEEE/CVF International Conference on Computer Vision, pp. 9433–9443.
- Zhu, H., Yuen, K.V., Mihaylova, L., Leung, H., 2017. Overview of environment perception for intelligent vehicles. IEEE Transactions on Intelligent Transportation Systems 18, 2584–2601.